

# Strain-enabled phase transition of periodic metasurfaces

Yu, Jiancan; Liu, Zhihua; Wang, Ming; Wang, Changxian; Chen, Geng; Cui, Zequn; Wang, Ting; Yang, Hui; Wang, Xiaotian; Chen, Xiaodong

2022

Yu, J., Liu, Z., Wang, M., Wang, C., Chen, G., Cui, Z., Wang, T., Yang, H., Wang, X. & Chen, X. (2022). Strain-enabled phase transition of periodic metasurfaces. *Advanced Materials*, 34(1), 2102560-. <https://dx.doi.org/10.1002/adma.202102560>

<https://hdl.handle.net/10356/156392>

<https://doi.org/10.1002/adma.202102560>

---

This is the peer reviewed version of the following article: Yu, J., Liu, Z., Wang, M., Wang, C., Chen, G., Cui, Z., Wang, T., Yang, H., Wang, X. & Chen, X. (2022). Strain-enabled phase transition of periodic metasurfaces. *Advanced Materials*, 34(1), 2102560-, which has been published in final form at <https://doi.org/10.1002/adma.202102560>. This article may be used for non-commercial purposes in accordance with Wiley Terms and Conditions for Use of Self-Archived Versions.

*Downloaded on 13 Mar 2024 18:55:53 SGT*

DOI: 10.1002/((please add manuscript number))

**Article type: Research Article**

## **Strain-enabled Phase Transition of Periodic Metasurfaces**

Jiancan Yu, Zhihua Liu, Ming Wang, Changxian Wang, Geng Chen, Zequn Cui, Ting Wang, Hui Yang, Xiaotian Wang, Xiaodong Chen\*

Dr. J. Yu, Dr. Z. Liu, Dr. M. Wang, Dr. C. Wang, Dr. G. Chen, Dr. Z. Cui, Dr. T. Wang, Dr. H. Yang, Dr. X. Wang, Prof. X. Chen\*

Innovative Centre for Flexible Devices (iFLEX), Max Planck – NTU Joint Lab for Artificial Senses, School of Materials Science and Engineering, Nanyang Technological University, Singapore 639798, Singapore

\*Email: [chenxd@ntu.edu.sg](mailto:chenxd@ntu.edu.sg)

Dr. J. Yu

School of Materials, Sun Yat-sen University, Shenzhen Campus, Shenzhen 518107, China

Dr. Z. Liu, Prof. X. Chen

Institute of Materials Research and Engineering, Agency for Science, Technology and Research (A\*STAR), 2 Fusionopolis Way, Innovis, #08-03, Singapore 138634, Singapore

**Keywords:** Phase transition, metasurfaces, Bravais lattices, strain engineering

**Abstract:** Phase transitions are universal in solid-state matters, as well as in periodic electromagnetic metasurfaces -- the photonic analogues of crystals. Although such transitions dictate the properties of active metasurfaces, universal ways to describe the structure transition of periodic metasurfaces have not yet been established. Here, we report the strain-enabled phase transition (or lattice deformation) of stretchable metasurfaces with the crystallographic description. We analytically and experimentally demonstrate the phase transition of plasmonic lattices between two arbitrary two-dimensional (2D) Bravais lattices under certain strain configurations. The strain-induced symmetry lowering of the structures gives rise to optical anisotropy upon polarization, namely, linearly and circularly polarized dichroism. We further demonstrate the potential of phase transition in information decoding with applied strain. Interpreting the phase transition of metasurfaces from a standpoint of symmetry would accelerate the discovery of emergent properties, and provide a generalizable approach to designing active metasurfaces.

## 1 Introduction

Electromagnetic metasurfaces offer ultrathin optical components ( $<$  the operating wavelength) essential for the miniaturization of photonic systems.<sup>[1-6]</sup> Metasurfaces comprise subwavelength elements that can form the contrast of permittivity or permeability to their surroundings in a geometric configuration. Such subwavelength elements are extracted as a model called meta-atoms, analogues of natural atoms, and metasurfaces operate like their analogues of solid-state matters.<sup>[2]</sup> This understanding is incessantly nourishing the field of metasurfaces. Among them, periodic metasurfaces, where meta-atoms are arranged in periodic lattices, are one of the most prevailing structures (Figure S1).<sup>[1, 7-12]</sup> Like natural crystals, periodic metasurfaces support two-dimensional (2D) Bragg modes due to long-range coherent interactions between meta-atoms, leading to strong dispersion of the effective permittivity or permeability, dependent on the geometry of lattices. As a result, metasurfaces with various 2D lattices offer a broad spectrum of interesting optical properties. The engineered dispersion yields high- $Q$  (quality factor) resonance reflection and/or absorption, and has enabled them to be ideal platforms for chemical sensing<sup>[11, 13]</sup> and the coupling with absorptive and excitonic materials.<sup>[11, 14-21]</sup> Furthermore, the frequency of emerging resonance sensitively depends on lattices' geometry and periodicity,<sup>[8, 13]</sup> offering accessible degrees of freedom to dynamically control the resonances of metasurfaces, and thus the regime of strong coupling. These degrees of freedom form the design principle for active metasurfaces, crucial for the photonic and communication systems.<sup>[22-25]</sup>

Active metasurfaces are driven in various ways, including electrical gating, optical pumping, mechanical actuation, etc.<sup>[24, 26, 27]</sup> Deformable metasurfaces, whose optical responses are directly tuned through spatially re-arrangement of meta-atoms by mechanical actuation, constitute a large category of active metasurfaces,<sup>[12, 28]</sup> which have benefitted from the maturation of micro-electro-mechanical (MEMS) systems. These optical responses result in functional mechanical reconfigurable metasurfaces, such as adaptive metalens,<sup>[28, 29]</sup> tunable holograms,<sup>[30]</sup> and variable gratings.<sup>[31]</sup> In particular, periodic lattices, which are inherently sensitive to the spacing between meta-atoms, have shown remarkable tuneability in structural colors and lasing wavelength under strains.<sup>[12, 32-35]</sup> Although the deformation of periodic metasurfaces under strain has been reported frequently,<sup>[12, 32-34]</sup> there remain no universal ways to describe strain-induced lattice deformation of periodic metasurfaces. As a result, one may neglect the accessible structures, and fail to discover interesting optical properties of metasurfaces under mechanical actuation.

Here, we report a universal way to access arbitrary phases of periodic metasurfaces by applying strains. We introduce the crystallographic terminology of 2D Bravais lattices,<sup>[36]</sup> which reflect the lattice symmetry, to describe the arrangement of meta-atoms. Together with geometrical analysis, we experimentally demonstrate the phase transition between two arbitrary 2D Bravais lattices. The strain-induced symmetry lowering of the structures gives rise to extinction anisotropy upon polarization, which agrees well with the symmetry of a lattice sum tensor<sup>[8]</sup> --a geometric factor of lattices. This idea of strain-enabled phase transition is further extended to the meta-atoms of an

elliptic cylinder shape. Considerable circular dichroism (ellipticity  $\sim 2$  degree) is observed experimentally in the mirror-lacking oblique lattices obtained from stretching the hexagonal lattice. Using the optical isotropic to anisotropic transition that relies on the initial orientation of lattices, we applied the strain-enabled phase transition of lattices to information decoding. These results provide fundamental insights into strain-induced symmetric control over periodic metasurfaces, which may offer design principles for mechanically active metasurfaces. More importantly, interpreting the strain-induced lattice deformation from the standpoint of symmetry would accelerate the discovery of emergent properties of periodic metasurfaces and the establishment of theoretical frameworks by learning from matured crystallography, solid-state physics and materials science.

## 2 Results and Discussion

We began with predicting the lattice deformation under a uniaxial strain according to basic geometric relations, where we assumed the particles attached to the lattices are rigid and non-deformable. As sketched in Figure 1a, after stretching the lattice along a certain direction, the coordinate of an individual particle embedded in an elastomer initially at position  $(x, y)^T$  is associated with a deformation gradient tensor<sup>[37]</sup> given by the following formula:

$$\begin{pmatrix} x' \\ y' \end{pmatrix} = R(\theta)FR(-\theta) \begin{pmatrix} x \\ y \end{pmatrix} \quad (1)$$

where  $R(\theta) = \begin{pmatrix} \cos \theta & -\sin \theta \\ \sin \theta & \cos \theta \end{pmatrix}$  is a rotational matrix,  $\theta$  is the intersection angle between the stretching direction and the positive direction of the  $x$ -axis, and  $F = \begin{pmatrix} \lambda_1 & 0 \\ 0 & \lambda_2 \end{pmatrix}$  is a deformation gradient tensor with the stretch ratio  $\lambda_1 = 1 + \varepsilon$  and  $\lambda_2 =$

$1/\sqrt{1 + \varepsilon}$ , here  $\varepsilon$  is the applied strain on the lattice and the elastomer is regarded as an ideal elastomer that conserves volume. Here the matrix  $R(\theta)FR(-\theta)$  is a linear operator on the coordinates of the particles, and therefore homogenously maps a periodic lattice (net) to another periodic one. Intuitively, the uniaxial stress leads to elongation of the elastomer, as well as increased spacing of particles along the stretching direction and compression in the perpendicular direction. Such difference gives rise to symmetry breaking.

We examined the phase transition of metasurfaces featuring hexagonal lattices under strain. The hexagonal lattice is basic among five 2D Bravais lattices, and ubiquitous in 2D natural crystals and artificial photonic crystals. It is also the only lattice that allows for the closest packing of circular atoms or meta-atoms in a planar configuration. Coincidentally, most 2D layered crystals, including graphene and  $\text{MoS}_2$ , adopt a honeycomb structure, which essentially belongs to the hexagonal Bravais lattice. The hexagonal lattice has two kinds of non-equivalent 6-fold axes of rotation, i.e.  $x$ - and  $y$ -axis (Figure 1a, left). Stretching the lattice along these rotational symmetric axes (corresponding to  $\theta = 0^\circ$  and  $90^\circ$ ) forms centered rectangular lattices, where the lengths of  $b$  and  $c$  sides remain equal (Figure 1b). Specifically, when stretching along the  $x$ -axis, the intersection angle ( $\alpha$ ) between  $b$  and  $c$  sides increases from  $60^\circ$  to  $90^\circ$  at a strain of 44%, and to  $120^\circ$  when  $\varepsilon = 101\%$ . These two special cases correspond to the square and extended hexagonal lattices, respectively, which are higher in symmetry than trivial rectangular ones and were not emphasized elsewhere to the best of our knowledge.<sup>[12]</sup>

Other accessible Bravais lattices can be obtained by stretching along nonsymmetric axes. As a general case of a square lattice, rectangular lattices can be obtained around the stretching condition  $(\theta, \varepsilon)$  for the square lattice, i.e.  $\varepsilon > 44\%$ , and each strain corresponds to 12 possible orientation angles that differ from one another by  $60n$  degree ( $n$  is an integer) or are reflective about the rotational axes (Figure 1c). For example, a rectangular lattice is obtained when stretching along  $\theta = 10^\circ$  and with a strain of 49% (Figure 1d). The oblique lattice, a general Bravais lattice with the least symmetric elements, can be obtained easily by stretching along non-symmetric axes of a hexagonal lattice with a trivial strain. For example, when the hexagonal lattice is stretched along  $\theta = 20^\circ$  with a strain of 32%, the lattice turns oblique. It is a special oblique lattice that forms a rectangular superlattice with three repeated cells (Figure S2). Nevertheless, it still falls in the oblique category according to the definition of Bravais lattice. Furthermore, by varying the strain configurations, ones are able to obtain all other four types of 2D Bravais lattices, which are summarized in a phase diagram (Figure 1c) and a set of representative examples (Figure 1d).

To experimentally demonstrate the phase transition of metasurfaces, we prepared hexagonal Au plasmonic lattices with a periodicity of 500 nm (the diameter of Au disks,  $\sim 140$  nm). At this scale, surface lattice resonances (SLRs) dominate at the visible to near-infrared (NIR) region,<sup>[9, 12]</sup> allowing lattice deformation to be readily tracked via spectral evolution. Plasmonic lattices of gold nanodisks were prepared by a standard electron-beam lithography procedure, and then transferred to a stretchable polydimethylsiloxane (PDMS) substrate (Figure 2a-b). The field emission scanning

electron microscopy (FESEM) image of Au lattices (Figure 2c) on sacrificial nickel layers shows that Au nanoparticles are uniform in size and are arranged in a hexagonal lattice with few defects (missing Au meta-atoms, less than 1%). Successful transfer from Si/Ni substrate to PDMS is confirmed by the optical micrograph of the transferred lattice (Figure S3), which reveals an almost defect-free structure over a large area.

We followed the evolution of the strained lattice under a microscope with an oil-immersion objective. When the PDMS sample is stretched, the hexagonal lattices undergo deformation conformably regardless of the stretching orientation. We tracked the lattice deformation when stretching it along the axes of symmetry. The parameters of the strained lattices show excellent agreement with the calculated results (Figure 1b), indicating that the lattice experiences the deformation as predicted. In this manner, four other types of 2D Bravais lattices were achieved under the appropriate strain configurations (Figure 2e-h). The Au particles were found to fall precisely within the sites of the calculated lattices (yellow circles in Figure 2e-h). The phase transition of the hexagonal metasurfaces is also reflected in the reciprocal space, which is revealed in the associated fast Fourier transform (FFT) patterns.

We further examined the phase transition from a relatively low-symmetric lattice, i.e. an oblique lattice, to four other types of Bravais lattices with higher symmetry. Starting with an oblique lattice as described in Figure 1d and 2h, four other Bravais lattices were achieved experimentally (Figure S4). In fact, one can obtain any other types of Bravais lattice from any kind of lattice simply by applying the uniaxial strain along a certain orientation (Table 1, Figure S5-7). These results demonstrate that strain-

enabled phase transition of metasurfaces can be achieved between any two different Bravais lattices. This comprehensive library of possible phase transitions provides a guide for exploring strain-induced phases of their atomic analogues, natural 2D crystals.<sup>[38]</sup>

Mechanical simulation using finite element methods (Figure S8) shows that Au nanoparticles embedded in the PDMS medium do not elongate or deform, and this is reasonable because of the significant difference in Young's modulus between gold and PDMS (79 GPa vs. 1.5-2 MPa<sup>[39]</sup>). We found that the upper surface plane of Au nanoparticles is protruded from the PDMS substrate by ~12 nm after applying a strain of 30%. Fortunately, the extruded Au nanoparticles still lie within the same plane, and therefore the protrusion of Au particles would not significantly weaken the plasmonic surface lattice resonance.

We tracked the spectral evolution during stretching along the rotational axes ( $\theta = 0$  and  $90^\circ$ ), which produces centered rectangular lattices (Figure 3a-e). The initial hexagonal lattice of Au nanoparticles shows a strong resonance peak at 683 nm upon normal incidence without polarization dependence, revealing the optical isotropic feature. As identified by simulation previously, both reflection ( $R$ ) and absorption ( $A$ ) contribute to the extinction ( $E$ ) at the resonance due to collective behavior.<sup>[9]</sup> When the hexagonal lattice is stretched along  $\theta = 90^\circ$ , the resonance peaks of the resultant lattices are significantly red-shifted under horizontal polarization (H-pol, perpendicular to the stretching direction), while the resonance peaks broaden slightly and are blue-shifted under vertical polarization (V-pol). The redshift of resonance peaks with the row

spacing of Au nanoparticles under V-pol resembles the case that 1D nanogratings support lower-energy mode at higher periodicities.<sup>[40]</sup> In another case of stretching along  $\theta = 0^\circ$ , the peak shift is smaller than those along  $\theta = 90^\circ$ , and a similar trend is observed under both vertical and horizontal polarization. It is worth mentioning that these spectra of stretched lattices are in excellent agreement with the simulation results (Figure S9) and predefined lattices that correspond to these strained lattices in geometry (Figure S10), suggesting that the stretched lattices are arranged exactly as calculated. This large and monotonous peak shift under vertical polarization can be regarded as a measure of strains (Figure 3e), forming the basis for ultrasensitive strain sensors,<sup>[41]</sup> as well as tunable lasers.<sup>[19, 32]</sup>

To reveal the role of lattice structures in the extinction properties of plasmonic lattices, we use the coupled dipole approximation (CDA) method to extract the geometric factor of the strained lattices undergoing deformation.<sup>[42]</sup> The effective polarizability of the Au nanoparticle in a periodic lattice is expressed with a lattice sum tensor according to

$$\boldsymbol{\alpha}_{\text{eff}} = \frac{1}{1/\alpha_{\text{NP}} - \mathbf{G}(0)} \quad (2)$$

where  $\alpha_{\text{NP}}$  is the polarizability of the individual Au nanoparticle,  $\mathbf{G}(0)$  is the lattice sum tensor in the case of normal incidence. In the case of isotropic Au nanodisks, the contribution of the geometrical factor,  $\mathbf{G}(0)$ , which reflects dipole-dipole interaction, shapes the symmetry of effective polarizability, as well as the extinction properties (see Supporting Information). Specifically, when the lattice sum  $\mathbf{G}(0)$  is diagonal, the effective polarizability is simplified as a diagonal tensor as follows:

$$\alpha_{\text{eff}} = \begin{pmatrix} \frac{1}{1/\alpha_{\text{NP}} - G_{xx}} & 0 \\ 0 & \frac{1}{1/\alpha_{\text{NP}} - G_{yy}} \end{pmatrix}$$

The lattice sum of the hexagonal lattice has been extensively investigated;<sup>[12]</sup> it is degenerated as a scalar because of the isotropic feature of the hexagonal lattice. Figure 3e shows that the real parts of the diagonal components,  $G_{xx}$  and  $G_{yy}$ , reach their equal maxima at the wavelength of  $\sqrt{3}an_m/2$ , where  $a$  ( $= 500$  nm) is the lattice constant and  $n_m = 1.4$  is the refractive index of the surrounding medium. Their imaginary parts (Figure S11) also show their maxima at around  $\sqrt{3}an_m/2$ , and the off-diagonal components identically equal 0. Importantly, the lattice sum shows extraordinarily steep dispersion near its peak, in contrast to the inverse of polarizability for the individual Au nanoparticle that shows weak dispersion over the entire vis-NIR region (see Figure S12). This striking difference between  $G$  ( $G_{xx}$  and  $G_{yy}$ ) and  $1/\alpha_{\text{NP}}$  at some specific frequency suggests the decisive role of lattice geometry in tuning the resonance frequency of lattices.

By stretching the hexagonal lattice along rotational axes (Figure 3a), the anti-diagonal elements the lattice sum vanish (Figure S13), but the two diagonal components no longer coincide (i.e.  $G_{xx} \neq G_{yy}$ , Figure 3f-g), with the lattice becoming centered rectangular. Such tensor property is responsible for the optical anisotropy upon polarization, shown spectrally in Figure 3f-g. Furthermore, the evolution of lattice sums shows a strong dependence on the stretching orientation. Stretching along  $\theta = 90^\circ$  (Figure 3e) shows significantly redshift in wavelengths for  $G_{xx}$  maxima and slightly blue-shifts for those of  $G_{yy}$ , and reduces the peak intensity, whereas the maxima of both

$G_{xx}$  and  $G_{yy}$  exhibit a moderate redshift during stretching along  $\theta = 0^\circ$  (Figure 3g). The considerable wavelength shift of  $G_{xx}$  for the stretching along  $\theta = 90^\circ$  roughly reflects the significant distance increase of the Au rows that lines along the  $x$ -axis.

We correlated the resonance peaks of lattices with the geometrical factor of lattices, lattice sum. Lorentz oscillator model suggests that the resonance occurs when the real part of electric susceptibility vanishes, which is equivalent to  $\text{Re}(\alpha_{\text{eff}}) = 0$  approximately in combination with the Clausius–Mossotti relation (see Supporting Information).<sup>[43]</sup> The condition can further be rephrased as the real part of  $(1/\alpha_{\text{NP}} - \mathbf{G}(0))$  vanishing (i.e.,  $\text{Re}(1/\alpha_{\text{NP}}) = \text{Re}(\mathbf{G}(0))$ ), visually corresponding to the intersection point of the  $1/\alpha_{\text{NP}}$  curve with the  $G$  plot. Here the components  $G_{xx}$  and  $G_{yy}$  are associated with the horizontally and vertically polarized excitation, respectively. This evolution of lattice sum with strain explains the redshift of resonance peaks in the transmission spectra, especially the considerable redshift for that stretched along  $\theta = 90^\circ$  under horizontally polarized excitation.

To further reveal the symmetry of optical properties, we correlated it with the symmetry of lattice sum tensors, which directly reflect the symmetry of lattices. According to the Clausius–Mossotti relation, the extinction properties of materials are determined by their macroscopic electric susceptibilities, which are ultimately determined by the microscopic electric polarizability, yielding the extinction coefficient  $K = \sqrt{\epsilon_m} N \text{Im}(\alpha_{\text{eff}})/2$  (see Supporting Information). This formula implies the symmetric similarity between the extinction property of a lattice and the corresponding lattice sum. As shown in Figure 4a and summarized in Table 2, there is only an

independent component ( $G_{xx} = G_{yy}$ ,  $G_{xy} = G_{yx} = 0$ ), in the lattice sum tensor for both the hexagonal and stretched square lattices. These tensors are therefore degenerated into a scalar, since the off-diagonal components always vanish no matter which principal axes are chosen, indicating an isotropic feature of the optical properties. It is also evident in the polarization-dependent transmission spectra and the corresponding polar plots of extinction (Figure 4e-f).

The lattice sums of rectangular lattices, both simple rectangular and centered rectangular, are diagonalizable over the entire visible frequency range, but with different diagonal entries (Figure S14-15). In the centered rectangular case, the candidates of the principal axes are exclusively the axes of symmetry, which are exactly along the sides of the rectangles (Figure 3a and S14). This diagonalizability feature and the choice of principal axes are indeed imposed by the symmetry of lattice structure according to Neumann's principle.<sup>[44]</sup> It is the same for simple rectangular lattice. Considering the scalar nature of polarizability for the circular nanoparticles, the effective polarizability would inherit such a diagonal feature of lattice sums. As a result, this symmetric feature of these tensors renders these rectangular lattices linearly polarized dichroism, which we discussed above (Figure 3c-d). For the centered rectangular lattices that are subject to strain along the axes of symmetry, the polarization-dependent transmission spectra (Figure 4f and i) show a two-fold symmetric profile with polarization, displaying the extinction maxima under the horizontally and vertically polarized excitation. A similar spectral feature is seen in the simple rectangular lattice (Figure S15). We can now conclude that stretching a

hexagonal plasmonic lattice induces property anisotropy by supporting two distinct surface lattice resonant modes of linear cross-polarization, which can be used to control the polarization of incident light and tune birefringence dynamically.

The oblique structure, which has the lowest symmetry among the five 2D Bravais lattices, was rarely employed in metasurfaces. In fact, the low symmetry is sometimes the physical origin of some extraordinary properties that are absent in materials and devices with high-symmetry structures.<sup>[44]</sup> As a property tensor, lattice sum is symmetric ( $G_{xy} = G_{yx}$ ) and diagonalizable in principle. Our calculation indicates that the lattice sum tensors of oblique lattices are exactly diagonalizable at any a specific wavelength, but fail to diagonalize over the entire frequency range (Figure S17), in strong contrast to other Bravais lattices. As a result, such an oblique structure supports two distinct resonance modes that are not linearly cross-polarized as the other four lattice types. This unique property may allow for polarization control more flexibly than other phases of higher symmetry.

The knowledge of crystal physics regarding structure-property relation leverages all periodic structures, and thus offers the common design principles for photonic structures with on-demand properties or strain-induced property evolution. To reveal new possibilities that the increased complexity of meta-atom offers, we used an elliptic cylinder-shaped Au nanoparticle as the basis of the hexagonal lattice (Figure S18 and Figure 5) to induce circular dichroism (CD) by applying strain on the initially hexagonal lattice. The purpose of using an elliptic cylinder instead of the circular disk is to further lower the symmetry of the resulting lattices. In this case, the initial hexagonal structure

no longer has six symmetric mirrors but two mirrors. The presence of a mirror indicates that there are no CD signals in the initial hexagonal lattice, which is reflected in the identical transmission spectra under both right-handed circular polarization (RCP) and left-handed circular polarization (LCP) incidence (Figure 5b). The lattice turns oblique (free of reflection symmetry) when it is stretched along  $\theta = 20^\circ$ . We investigated the spectral evolution experimentally, and found distinct spectral differences between RCP and LCP when  $\varepsilon = 10\%$ , which leads to an obvious CD signal at 640 nm (Figure 5b-c). The CD signals become stronger and are extended to the NIR region when strain increased, with the largest ellipticity of  $\sim 2$  degree. Such strong CD responses are well consistent with the simulated results (Figure S19), while the discrepancy between experimental and simulated results could be attributed to the fabrication accuracy of Au nanoparticles. However, as expected, no significant CD responses are observed for the lattices under the uniaxial strain along these symmetric axes, e.g. along  $\theta = 0$  or  $90^\circ$ . The occurrence of significant CD can be interpreted as the synergetic interplay between asymmetric lattice and elliptical nanoparticles (basis) that ultimately determines the effective electric/magnetic polarizability. The peak shift of CD signals of lattices with various periodicity indicated a crucial role in the emergence of CD response (Figure S20). To the best of our knowledge, the circular dichroism induced by lattices without reflection symmetry was not reported elsewhere.

Metasurfaces have been explored for encryption under various external activation.<sup>[45, 46]</sup> In our case, the unique strain-induced absorption and reflection evolution promise to decode with the mechanical strains. The isotropic optical

properties of the hexagonal lattice ensure the domains with various orientations to be indiscernible macroscopically in the initial state, no matter under natural light or a certain polarization, allowing to encode information pattern within the background. Upon stretching, the hexagonal lattices undergo a phase transition to other types of lattices, which depend on the initial orientation, leading to the difference in absorption and reflection. Such strain-induced difference forms a strong contrast between information and the background, and the information is decoded. For example, we embedded a pattern of 'NTU MSE' characters in a  $100 \times 100\text{-}\mu\text{m}^2$  region of the hexagonal lattice, where the background is with horizontal rows but the embedded pattern with vertical rows (with an orientation difference of  $90^\circ$ , Figure 6a-b). We recorded the image evolution of the square area while stretching the sample; considerable contrast in both the reflection and extinction was observed (Supporting Video 1 and 2) once the strain reaches around 15%. Specifically, the green pattern is observed against the brownish background in a transmission mode under the vertical polarization, whereas the pattern is unclear under horizontal polarization. Although the spectra between the pattern and background are radically different, the observed slight contrast results from the resonance occurring in the red to NIR region, which is not sensitive to the naked eye and common cameras. Fortunately, strong contrast forms after stretching with a strain  $>15\%$  under the reflected and reflected differential interference contrast (DIC) mode (Figure 6d, S21), offering a practical way to decipher the hidden information by applying strain.

Finally, we evaluated the stability of the lattices during stretch-release cycling. As shown in the transmission spectra (Figure S22), the peak wavelengths for the resonance of the plasmonic lattices almost remain after repetitive strain with the maximal strain = 20% or 40% both for the released or the stretched states. However, the resonance strength (corresponding to the transmittance) turns a little weaker after a relatively large repeated strain of 40%, which is more evident for the strained lattice (Figure S22b-c). The spectral evolution can be attributed to the inhomogeneous extrusion of Au nanoparticles, which is reflected in the topographic images of atomic force microscopy (AFM). In Figure S23, the Au nanoparticles in the as-prepared sample are slightly extruded from the PDMS substrates uniformly, while inhomogeneous topography of nanoparticles is observed after repeated stretch-release cycling. In this case, the stability of stretchable metasurface could be further improved by covering an additional PDMS layer on the Au lattices so that the Au nanoparticles are well confined in the PDMS substrate.

### 3 Conclusions

In summary, we demonstrated the strain-induced phase transition of periodic metasurfaces theoretically and experimentally. With a hexagonal lattice embedded in elastomer, we obtained all five types of 2D Bravais lattices simply under an appropriate strain configuration. We further showed that this approach works for transition between any two 2D Bravais lattices, which forms a comprehensive crystallography library for exploring strain-induced phases of natural atomic 2D crystals.<sup>[46]</sup> The strain-induced

symmetry lowering of the structures gives rise to linear and circular dichroism. Notably, the correlation between structure and optical properties is governed by lattice sum tensors, facilitating the structure design and property prediction of periodic metasurfaces. We anticipate that strain-induced symmetry control over metasurfaces would provide a dynamic platform for local electromagnetic field control, which is essential to exploring the coupling between metasurfaces and low-dimension materials.

### **Supporting Information**

Supporting Information is available from the Wiley Online Library or from the author.

### **Acknowledgements**

This work was supported by Singapore Ministry of Education (MOE2017-T2-2-107 and MOE2019-T2-2-022) and the National Research Foundation (NRF), Prime Minister's Office, Singapore, under its NRF Investigatorship (NRF-NRFI2017-07). We also thank Q. Lei and A. Li for assistance in simulation.

### **Conflict of Interest**

The authors declare no conflict of interest.

### **Data Availability Statement**

The data are available from the corresponding author upon reasonable request.

Received: ((will be filled in by the editorial staff))  
Revised: ((will be filled in by the editorial staff))  
Published online: ((will be filled in by the editorial staff))

## References

- [1] N. Meinzer, W. L. Barnes, I. R. Hooper, *Nat. Photon.* **2014**, 8, 889.
- [2] N. Yu, F. Capasso, *Nat. Mater.* **2014**, 13, 139.
- [3] A. V. Kildishev, A. Boltasseva, V. M. Shalaev, *Science* **2013**, 339, 1232009.
- [4] A. Li, S. Singh, D. Sievenpiper, *Nanophotonics* **2018**, 7, 989.
- [5] H.-H. Hsiao, C. H. Chu, D. P. Tsai, *Small Methods* **2017**, 1, 1600064.
- [6] P. Cheben, R. Halir, J. H. Schmid, H. A. Atwater, D. R. Smith, *Nature* **2018**, 560, 565.
- [7] L. Zhao, K. L. Kelly, G. C. Schatz, *J. Phys. Chem. B* **2003**, 107, 7343.
- [8] F. J. García de Abajo, *Rev. Mod. Phys.* **2007**, 79, 1267.
- [9] B. Auguié, W. L. Barnes, *Phys. Rev. Lett.* **2008**, 101, 143902.
- [10] W. Zhou, T. W. Odom, *Nat. Nanotechnol.* **2011**, 6, 423.
- [11] A. Tittl, A. Leitis, M. Liu, F. Yesilkoy, D.-Y. Choi, D. N. Neshev, Y. S. Kivshar, H. Altug, *Science* **2018**, 360, 1105.
- [12] A. Yang, A. J. Hryn, M. R. Bourgeois, W.-K. Lee, J. Hu, G. C. Schatz, T. W. Odom, *Proc. Natl. Acad. Sci. U. S. A.* **2016**, 113, 14201.
- [13] B. Špačková, J. Homola, *Opt. Express* **2013**, 21, 27490.
- [14] G. Vecchi, V. Giannini, J. Gómez Rivas, *Phys. Rev. Lett.* **2009**, 102, 146807.
- [15] A. H. Schokker, A. F. Koenderink, *Phys. Rev. B* **2014**, 90, 155452.
- [16] K. Kumar, H. Duan, R. S. Hegde, S. C. W. Koh, J. N. Wei, J. K. W. Yang, *Nat. Nanotechnol.* **2012**, 7, 557.
- [17] W. Zhou, M. Dridi, J. Y. Suh, C. H. Kim, D. T. Co, M. R. Wasielewski, G. C. Schatz, T. W. Odom, *Nat. Nanotechnol.* **2013**, 8, 506.
- [18] J. Olson, A. Manjavacas, L. Liu, W.-S. Chang, B. Foerster, N. S. King, M. W. Knight, P. Nordlander, N. J. Halas, S. Link, *Proc. Natl. Acad. Sci. U. S. A.* **2014**, 111, 14348.
- [19] D. Wang, W. Wang, M. P. Knudson, G. C. Schatz, T. W. Odom, *Chem. Rev.* **2017**, 118, 2865.
- [20] T. T. Tran, D. Wang, Z.-Q. Xu, A. Yang, M. Toth, T. W. Odom, I. Aharonovich, *Nano Lett.* **2017**, 17, 2634.
- [21] T. K. Hakala, A. J. Moilanen, A. I. Väkeväinen, R. Guo, J.-P. Martikainen, K. S. Daskalakis, H. T. Rekola, A. Julku, P. Törmä, *Nat. Phys.* **2018**, 14, 739.
- [22] L. Li, T. J. Cui, W. Ji, S. Liu, J. Ding, X. Wan, Y. B. Li, M. Jiang, C.-W. Qiu, S. Zhang, *Nat. Commun.* **2017**, 8, 197.
- [23] L. Cong, P. Pitchappa, C. Lee, R. Singh, *Adv. Mater.* **2017**, 29, 1700733.
- [24] A. M. Shaltout, V. M. Shalaev, M. L. Brongersma, *Science* **2019**, 364, 3100.
- [25] L. Kang, R. P. Jenkins, D. H. Werner, *Adv. Opt. Mater.* **2019**, 7, 1801813.
- [26] S. Zhang, *Light Sci. Appl.* **2020**, 9, 94.

- [27] Y. Wang, C. Zhao, J. Wang, X. Luo, L. Xie, S. Zhan, J. Kim, X. Wang, X. Liu, Y. Ying, *Sci. Adv.* **2021**, 7, eabe4553.
- [28] A. She, S. Zhang, S. Shian, D. R. Clarke, F. Capasso, *Sci. Adv.* **2018**, 4, eaap9957.
- [29] H.-S. Ee, R. Agarwal, *Nano Lett.* **2016**, 16, 2818.
- [30] S. C. Malek, H.-S. Ee, R. Agarwal, *Nano Lett.* **2017**, 17, 3641.
- [31] L. Xu, X. Wang, Y. Kim, T. C. Shyu, J. Lyu, N. A. Kotov, *ACS Nano* **2016**, 10, 6156.
- [32] J.-H. Choi, Y.-S. No, J.-P. So, J. M. Lee, K.-H. Kim, M.-S. Hwang, S.-H. Kwon, H.-G. Park, *Nat. Commun.* **2016**, 7, 11569.
- [33] S. Song, X. Ma, M. Pu, X. Li, K. Liu, P. Gao, Z. Zhao, Y. Wang, C. Wang, X. Luo, *Adv. Opt. Mater.* **2017**, 5, 1600829.
- [34] D. Wang, M. R. Bourgeois, W.-K. Lee, R. Li, D. Trivedi, M. P. Knudson, W. Wang, G. C. Schatz, T. W. Odom, *Nano Lett.* **2018**, 18, 4549.
- [35] J. Teyssier, S. V. Saenko, D. van der Marel, M. C. Milinkovitch, *Nat. Commun.* **2015**, 6, 6368.
- [36] C. Kittel, *Introduction to Solid State Physics*, John Wiley & Sons, Hoboken, 2004.
- [37] E. H. Dill, *Continuum Mechanics: Elasticity, Plasticity, Viscoelasticity*, CRC Press, Boca Raton, 2007.
- [38] Z. Dai, L. Liu, Z. Zhang, *Adv. Mater.* **2019**, 31, 1805417.
- [39] I. D. Johnston, D. K. McCluskey, C. K. L. Tan, M. C. Tracey, *J. Micromech. Microeng.* **2014**, 24, 035017.
- [40] Y. Hua, A. K. Fumani, T. W. Odom, *ACS Photonics* **2019**, 6, 322.
- [41] W. Chen, W. Liu, Y. Jiang, M. Zhang, N. Song, N. J. Greybush, J. Guo, A. K. Estep, K. T. Turner, R. Agarwal, C. R. Kagan, *ACS Nano* **2018**, 12, 10683.
- [42] V. G. Kravets, A. V. Kabashin, W. L. Barnes, A. N. Grigorenko, *Chem. Rev.* **2018**, 118, 5912.
- [43] J. D. Jackson, *Classical Electrodynamics*, Wiley, Hoboken, 1998.
- [44] R. E. Newnham, *Properties of Materials: Anisotropy, Symmetry, Structure*, Oxford University Press, New York, 2005.
- [45] M. Z. Alam, S. A. Schulz, J. Upham, I. De Leon, R. W. Boyd, *Nat. Photon.* **2018**, 12, 79.
- [46] G. Qu, W. Yang, Q. Song, Y. Liu, C.-W. Qiu, J. Han, D.-P. Tsai, S. Xiao, *Nat. Commun.* **2020**, 11, 5484.

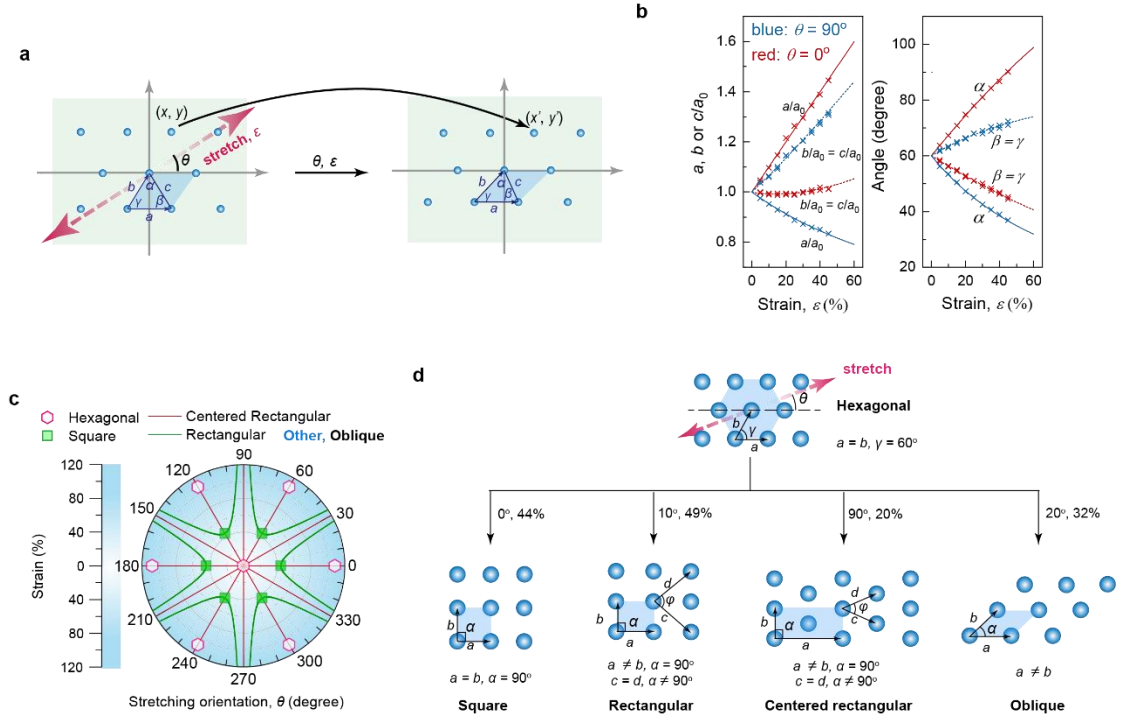


**Figure 1. Lattice deformation under strain.** a) Schematic of hexagonal lattice deformation under strain. The coordinate transformation of a point mass embedded in an ideal elastomer is given by  $\begin{pmatrix} x' \\ y' \end{pmatrix} = R(\theta)FR(-\theta) \begin{pmatrix} x \\ y \end{pmatrix}$ , where  $\begin{pmatrix} x' \\ y' \end{pmatrix}$  is the coordinate of a certain point mass located at  $\begin{pmatrix} x \\ y \end{pmatrix}$  after stretching along the angle of  $\theta$ . b) Cell constants of lattices stretched along  $0^\circ$  and  $90^\circ$  with strains ( $\epsilon$ ). The parameters are defined in (a). Cross, experimental data; line, calculated. c) Phase diagram of an initially hexagonal lattice under strain configuration (in the orientation-strain plane) shows 6-fold symmetry about the stretching orientation angle of  $\theta$ . d) Representative examples experiencing phase transition from the hexagonal lattice. Four other types of 2D Bravais lattices are achieved from the hexagonal one simply by stretching the elastomer. Note that the cell parameters in (d) are re-defined according to the symmetry of Bravais lattices.

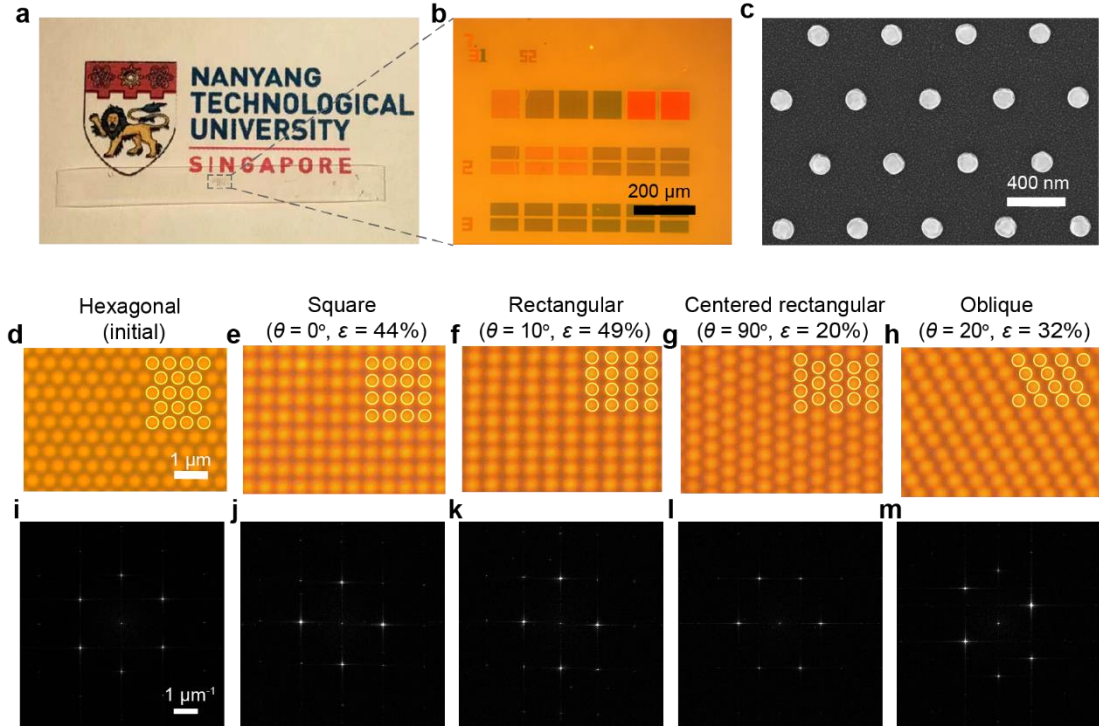


**Figure 2. Experimental realization of strain-enabled phase transition of plasmonic lattices.** a) Photo and (b) micrograph of Au nanoparticle lattices embedded in the elastic PDMS substrate, and (c) zoom-in FESEM image and (d) micrograph of Au hexagonal lattice ( $a = 500$  nm) imaged using an oil-immersion objective. e-h) Representative micrographs of four types of Au lattices obtained by stretching the hexagonal lattice in (d). i-m) Corresponding FFT patterns for micrographs in (d-h). FFT was performed on the grayscale micrographs ( $26 \times 26$  nm<sup>2</sup>,  $1200 \times 1200$  pixel<sup>2</sup>).

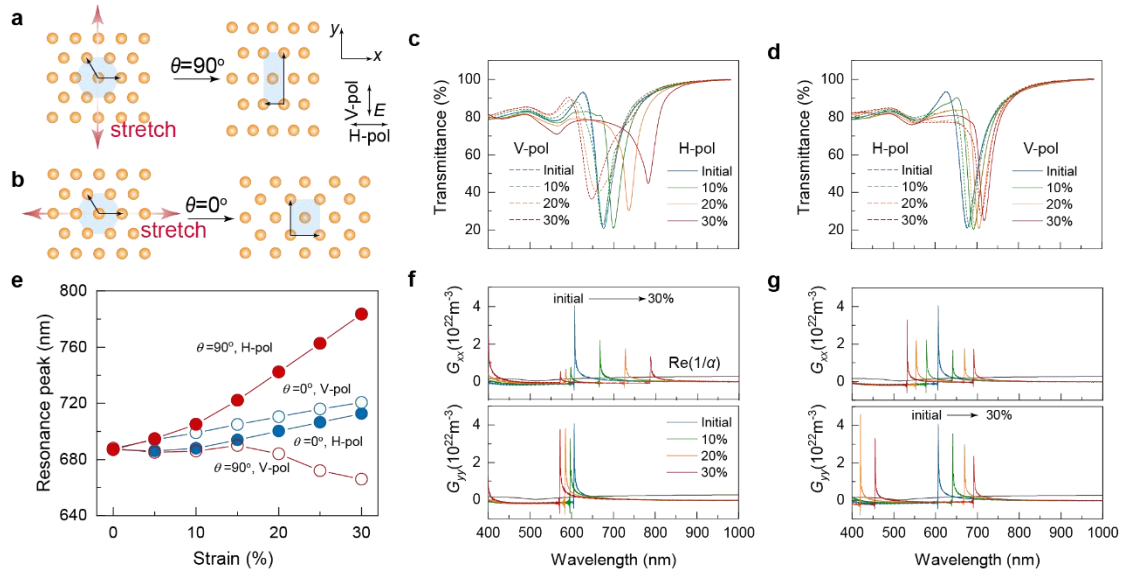


**Figure 3. Lattice deformation under strain along symmetric axes.** a-d) Schematic arrangement of Au nanoparticles under strains along  $\theta = 90^\circ$  (a) and  $\theta = 0^\circ$  (b), and the corresponding experimental transmission spectra (c, d). e) Wavelength evolution of the strongest resonance peaks for plasmonic lattices under various strain configurations. f, g, Real parts of the diagonal components of lattice sums that are subject to strains along  $\theta = 90^\circ$  (f) and  $\theta = 0^\circ$  (g). The subscripts of lattice sum tensors are defined by the frame of axes shown in (a-b). The coincidence between lattice sum and the inverse of the polarizability of Au nanoparticles yields surface lattice resonances.

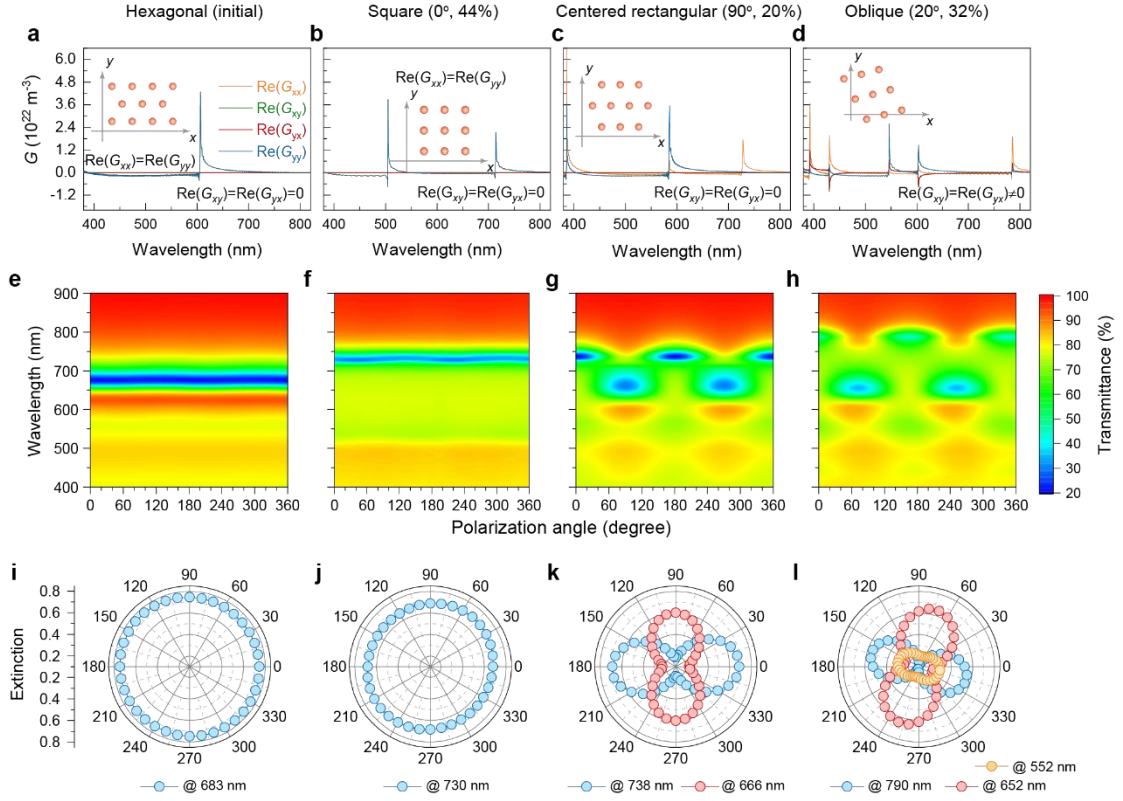


**Figure 4. Correlating the symmetry of lattice sum tensor with experimental spectra.** a-d) Real parts of the components of lattice sum tensors for hexagonal lattice (a) and other types of Bravais lattices derived from stretching (b-d). Inset: the lattices and corresponding coordinate systems. The structures of lattice sum tensors are summarized in Table 2. e-h) Polarization-dependent transmission spectra and (i-l) the corresponding polar plots of extinction for the hexagonal and stretched lattices, where extinction  $E=1-T$ , here  $T$  represents the transmittance.

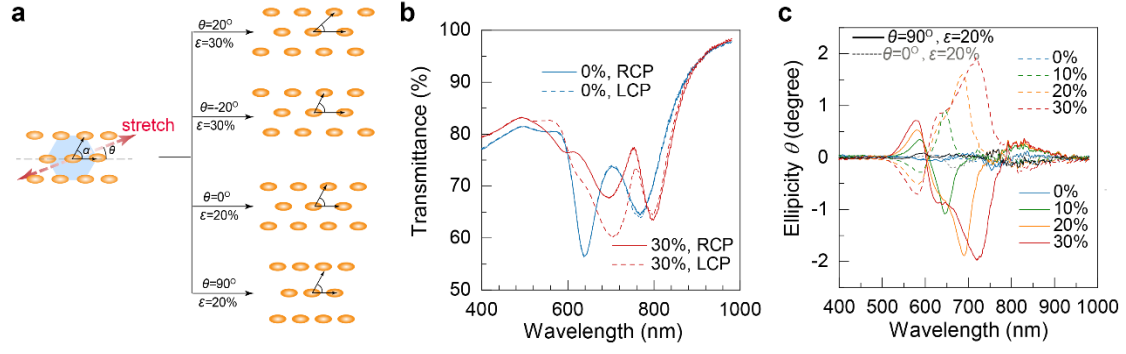


**Figure 5. Circular dichroism induced by the breaking of reflection symmetry.** a) Geometry of Au lattices with elliptic cylinder shape under various strain configurations. The lattices stretched along the orientation  $\theta = 20^\circ$  are oblique without reflection (or mirror) symmetry, while the lattices remain reflection symmetric when they are stretched along the symmetric axes. b) Experimental transmission spectra upon LCP and RCP light incidence, and (c) circular dichroism spectra evolution of plasmonic lattices during stretching.

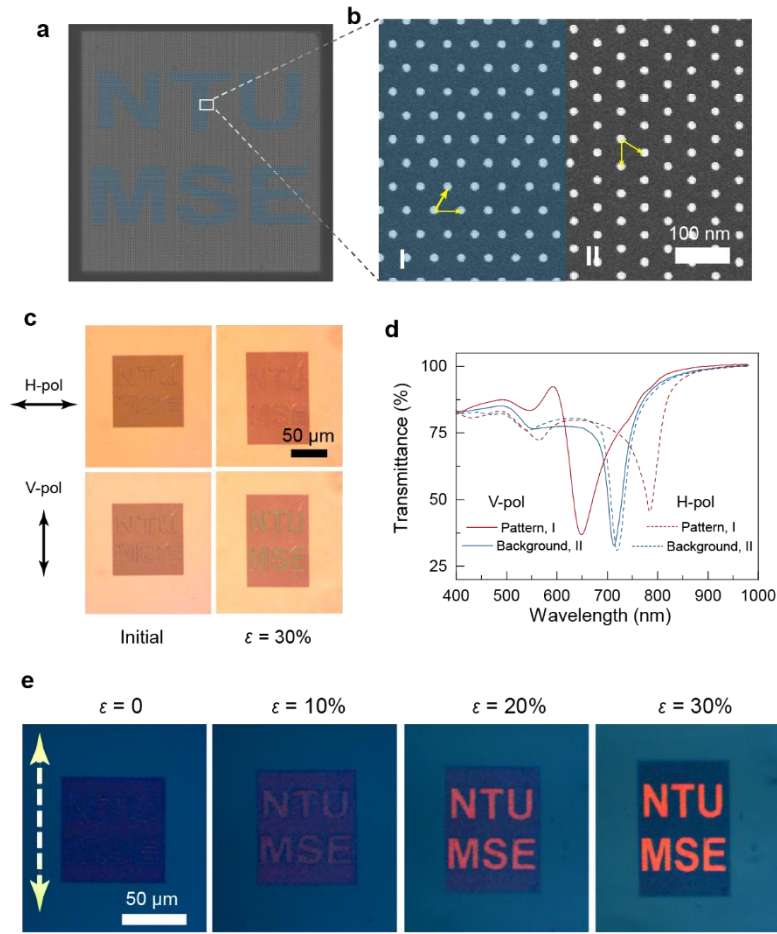


**Figure 6. Deciphering embedded domain of different orientation by strain.** a) FESEM image of hexagonal lattices embedded with an ‘NTU MSE’ pattern having domains of different orientations. The blue shadow indicates the region of the pattern rather than a physical entity. b) Zoom-in image shows the orientations. c) Micrographs of initial and stretched lattices under horizontal and vertical polarization. The presence of slight traces of the characters on the left panels can be attributed to the interruption of periodic structure of Au lattice at the domain boundary, which can be deliberately designed randomly (corresponding to amorphous phase) to alleviate or eliminate the effect. d) Experimental transmission spectra of stretched lattices ( $\epsilon = 30\%$ ). Transmittance difference under vertical polarization yields the contrast. e) Reflected DIC images of the hexagonal lattice with the embedded domain during stretching. The surrounding brightening is caused by the light scattering of the patterns. The arrows indicate the stretching direction.

**Table 1. Lattice constants for strain-enabled Bravais lattice deformation<sup>a</sup>**

Type of initial lattice	Lattice parameters				Deformation condition		Type of obtained lattice	Lattice parameters			
	Designed		Measured		Stretching orientation (°)	Strain (%)		Calculated		Measured	
	Lattice constant (nm)	$\alpha$ (°)	Lattice constant (nm)	$\alpha$ (°)				Lattice constant (nm)	$\alpha$ (°)	Lattice constant (nm)	$\alpha$ (°)
Hexagonal	$a = b = 500$	60	$a = 501$ $b = 505$	60	0	44	Square	$a = b = 510$	90	$a = 511, b = 512$	90
					10	49	Rectangular	$a = 573, b = 462$	90	$a = 572, b = 462$	89
					90	20	Centered rectangular	$a = 1039, b = 456$	90	$a = 1036, b = 463$	90
					20	31	Oblique	$a = 633, b = 575$	43	$a = 632, b = 581$	43
Square	$a = b = 500$	90	$a = 500$ $b = 507$	90	45	44	Hexagonal	$a = b = 588$	60	$a = 597, b = 586$	60
					0	20	Rectangular	$a = 600, b = 456$	90	$a = 600, b = 461$	90
					45	16	Centered rectangular	$a = 820, b = 657$	90	$a = 826, b = 661$	89
					70	26	Oblique	$a = 684, b = 471$	61	$a = 689, b = 473$	61
Rectangular	$a = 600$ $b = 400$	90	$a = 600$ $b = 407$	91	65	59	Hexagonal	$a = b = 591$	60	$a = 585, b = 600$	60
					90	31	Square	$a = b = 524$	90	$a = 526, b = 529$	90
					57	36	Centered rectangular	$a = 1134, b = 493$	90	$a = 1142, b = 499$	90
					60	21	Oblique	$a = 657, b = 596$	42	$a = 665, b = 599$	42
Centered rectangular	$a = 1092$ $b = 480$	90	$a = 1103$ $b = 483$	91	90	20	Hexagonal	$a = b = 576$	60	$a = 569, b = 573$	60
					90	72	Square	$a = b = 586$	90	$a = 584, b = 584$	89
					45	37	Rectangular	$a = 560, b = 548$	90	$a = 557, b = 547$	90
					102	52	Oblique	$a = 718, b = 508$	62	$a = 708, b = 509$	63
Oblique	$a = 636$ $b = 445$	62	$a = 638$ $b = 451$	62	76	32	Hexagonal	$a = b = 574$	60	$a = 571, b = 577$	61
					32	27	Square	$a = b = 530$	90	$a = 523, b = 540$	90
					20	20	Rectangular	$a = 565, b = 481$	90	$a = 564, b = 477$	90
					84	54	Centered rectangular	$a = 1187, b = 520$	90	$a = 1192, b = 522$	90

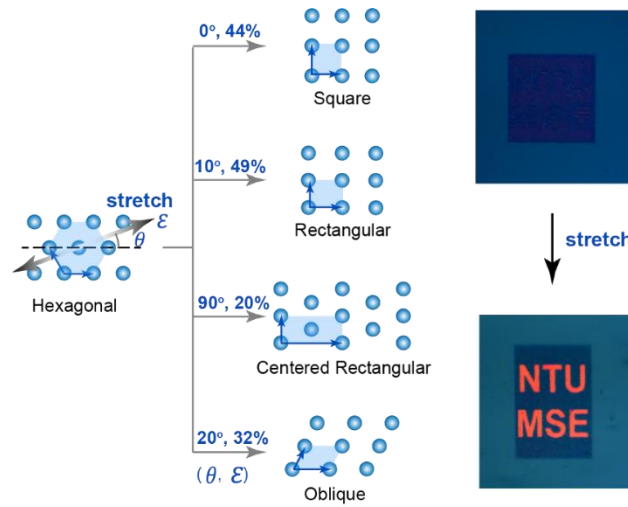
<sup>a</sup> Parameters are defined in Figure 1d and Figure S4-7.

**Table 2. Components of lattice sum tensors for various Bravais lattices.**

Lattice type	Component of $G(0)$
Hexagonal	$G_{xx} = G_{yy}; G_{xy} = G_{yx} = 0$
Square	
Rectangular	$G_{xx} \neq G_{yy}; G_{xy} = G_{yx} = 0$
Centered rectangular	
Oblique	$G_{xx} \neq G_{yy}; G_{xy} = G_{yx} \neq 0$ <sup>a</sup>

<sup>a</sup> Note  $G_{xy}$  and  $G_{yx}$  are not identically vanishing.

## The table of contents



**Strain-enabled phase transition** of stretchable periodic metasurfaces between any two Bravais lattices, which reflect their symmetry, is demonstrated analytically and experimentally. Such transition offers a flexible way to engineer the resonance regime and dispersion relation of metasurfaces. In particular, the strain-induced symmetry lowering leads to linearly and circularly polarized dichroism, which is demonstrated for information decoding.

## Keywords

Phase transition, metasurfaces, Bravais lattices, strain engineering

## Strain-enabled Phase Transition of Periodic Metasurfaces

Jiancan Yu, Zhihua Liu, Ming Wang, Changxian Wang, Geng Chen, Zequn Cui, Ting Wang, Hui Yang, Xiaotian Wang, Xiaodong Chen\*